

Chemical Science

Accepted Manuscript



This is an *Accepted Manuscript*, which has been through the Royal Society of Chemistry peer review process and has been accepted for publication.

Accepted Manuscripts are published online shortly after acceptance, before technical editing, formatting and proof reading. Using this free service, authors can make their results available to the community, in citable form, before we publish the edited article. We will replace this *Accepted Manuscript* with the edited and formatted *Advance Article* as soon as it is available.

You can find more information about *Accepted Manuscripts* in the [Information for Authors](#).

Please note that technical editing may introduce minor changes to the text and/or graphics, which may alter content. The journal's standard [Terms & Conditions](#) and the [Ethical guidelines](#) still apply. In no event shall the Royal Society of Chemistry be held responsible for any errors or omissions in this *Accepted Manuscript* or any consequences arising from the use of any information it contains.

ARTICLE

Photoelectrochemical Device Based upon Mo-doped BiVO_4 Enable Smart Analysis of Global Antioxidant Capacity in Food†

Cite this: DOI: 10.1039/x0xx00000x

Lingnan Wang,^{ab} Dongxue Han,^{*a} Shuang Ni,^{ac} Weiguang Ma,^{ab} Wei Wang^a and Li Niu^aReceived 00th January 20xx,
Accepted 00th January 20xx

DOI: 10.1039/x0xx00000x

www.rsc.org/

Healthy diet, an extension of a high quality lifestyle, has focused tremendous attention on its own antioxidant capacity indicators as food inspections and health guides. Albeit photoelectrochemical transducer broadening our horizon for global antioxidant activity analysis, a growing body of foods or beverages need to be quantified in the visible region whereas the concerned photoelectrochemical instrumentalization is still in infancy. Generally, BiVO_4 is considered as an ideal starting material for antioxidant surveillance under visible light irradiation. However, it is subjected to unsatisfied charge collection and utilization in practical applications. Herein, we lucubrated effects of successive molybdenum substitution of vanadium on photocatalytic behavior of $\text{BiMo}_x\text{V}_{(1-x)}\text{O}_4$ under visible-light illumination. A superior photocurrent density was obtained for $\text{BiMo}_{0.015}\text{V}_{0.985}\text{O}_4$ in view of the flower-like architecture and favorable crystalline form. At the same time, this superhybrid $\text{BiMo}_{0.015}\text{V}_{0.985}\text{O}_4$ composite successfully acted as sensing elements into a photoelectrochemical platform for antioxidant capacity evaluation in foodstuffs. The related mechanism was further unearthed and in-depth discussed. Such a straightforward yet cogent principle is also applied in our integrated device for the “smart” analysis of global antioxidant capacity, whereby collection data can be treated as a nutritive value index for routine quality control in food fields. On the basis of this achievement, it is anticipated that mobile app-based quantitative antioxidant capacity detection will soon come true.

Introduction

Drawing inspiration from healthy diet, antioxidant capacity (AC) based on antioxidative substances in fresh fruits and vegetables has spurred intense interest to evolve as a reliable index which should be a criterion for comparison and classification of foodstuffs, even providing quality standards for regulatory issues and health claims.¹ Recently, antioxidant nutrient content claims have been established as the guidance for industry in food labeling by the Food and Drug Administration (FDA, USA), which indicated that food AC analysis has received a comprehensive attention. Among well-established methods, photoelectrochemical (PEC) technique is considered to be an ideal platform for global AC assessment owing to its instinct mechanism, portability, high sensitivity and prominent anti-interference.² To deliver a sophisticated PEC system, eminent photoactive materials ought to possess proper band edge positions, band gap energies and pleasurable photostability.³ In particular, the conduction and valence bands

of preferential semiconductor should embrace the redox potentials of overall natural antioxidants (AOs), which give the possibility to make photo-induced holes reacting with all AOs. Of multitudinous semiconductors, n-type metal oxides become the most sought-after candidates for food inspections, since they are moderate cost, abundance, eco-friendly, corrosion resistance and possess highly reactive holes. Bearing these in mind, advanced TiO_2 -based nanomaterials appear to be benchmark material for dietary evaluation.⁴ Yet, the broad band gap in bare TiO_2 entails a limited PEC performance in the actual utilization.⁵ To our knowledge, shifting optical absorption threshold into the visible region would not only bring a breakthrough in photoresponse, but also cut cost for apparatus construction.

Accompanying by the emergence of ternary metal oxide BiVO_4 , it is deemed to be a valid alternative semiconductor in visible light harvesting.⁶ It is worth mentioning that morphology plus microstructure profoundly impact on BiVO_4 properties.⁷ There are three typically known polymorphs of

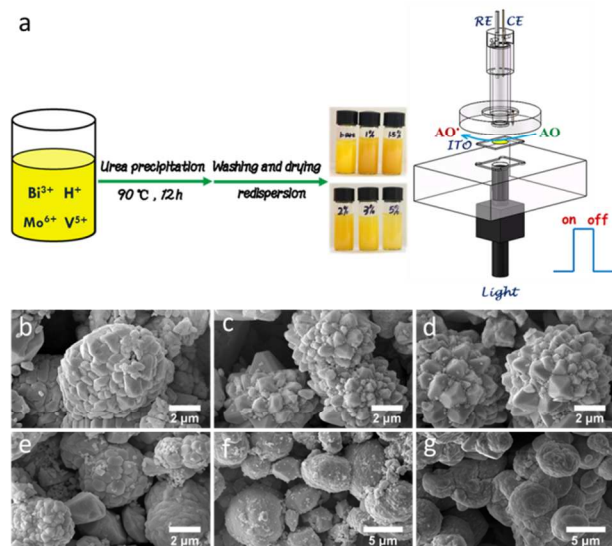


Fig. 1 a) Schematic illustration for preparation of $\text{BiMo}_x\text{V}_{(1-x)}\text{O}_4$ and the PEC process for AC assay. FESEM images of $x =$ b) 0, c) 0.01, d) 0.015, e) 0.02, f) 0.03 and g) 0.05 for $\text{BiMo}_x\text{V}_{(1-x)}\text{O}_4$.

BiVO_4 found in nature, monoclinic scheelite, tetragonal scheelite and tetragonal zircon, with the monoclinic scheelite structure exhibiting the best photocatalytically activity.⁸ Unfortunately, the actual photocatalytic behavior achieved with pristine BiVO_4 is far below expected, which imputes to its inferior charge-carrier separation and poor surface absorption.⁹ To circumvent this bottleneck, impurity doping of metal and nonmetallic elements into BiVO_4 seems to be a hot-spot strategy which can regulate the composition to further modify its optoelectronic efficiency. For instance, appending molybdenum to replace the partial sites of vanadium was found to enhance electronic conductivity and ultimately reduce the likelihood of electron-hole recombination in the bulk.¹⁰ Quite interesting, VO_4 units in the scheelite-type BiVO_4 are isolated, which drive the photogenerated electrons hopping between V neighbors since the conduction band (CB) makes the primary contribution from V3d orbitals.¹¹ Through displacing vanadium by high-oxidation state molybdenum provokes crystal deformation and polarons transport, thus upscaling charge carrier extraction efficiency.¹² Nevertheless, dopants can also be a double-edged sword, either exhibiting superior photocurrent density or tipping balance as scattering centers when the recommended ratio exceeded.¹³ Meanwhile, differences in the transport properties could not rely solely on heteroatoms, special surface feature from diverse fabrication routes play a key role in compensating self-trapping.¹⁴ Till now, the close relationship between structure transformation and variation in PEC properties has not been thoroughly discussed in research.

Here we report a one-pot chemical synthesis of $\text{BiMo}_x\text{V}_{(1-x)}\text{O}_4$, in which substituting lattice V with Mo brought distinct changes in crystal structure and optical absorption. In depth, the corresponding interrelation was adequately explored, given a better understanding of doped BiVO_4 systems. With the

appropriate doping, the exquisite PEC platform has been designed towards rationally estimating AC (Fig. 1a). Upon this framework, an integrated device for smart monitoring of AC in food has been successfully developed. Hereafter, such a portable, easy-to-use and cost effective bioassay equipment offers unrivalled convenience for consumers in well balancing nutrition.

Results and discussion

Engineering the expected PEC platform mostly included two straightforward procedures: 1) synthesis of tunable Mo-doped BiVO_4 via urea-precipitation reaction; 2) manipulating optimization composition in term of their property-to-performance trends (Fig. 1a). The series of field emission scanning electron microscopy (FESEM) images in Figure 1b-g reveal the diverse morphology along with the increase of Mo content. It is observed that bulk BiVO_4 presents loose microspheres and smooth surface (Fig. 1b). When Mo mole fraction [i.e., mol (Mo) per mol (Mo + V) = 0.015] is less or equal to 1.5%, a large number of protuberances were formed, resulting in visually flower-like architecture (Fig. 1c,d). Concomitantly improvements in surface active sites may breed on the localized gibbous topographies. Instead, higher doped proportion (>1.5%) suffered serious aggregation, which dramatically decreased its surface-to-volume properties (Fig. 1e-g) as well as water solubility (Fig. 1a).

The X-ray diffraction (XRD) analysis was conducted to investigate phase structure of $\text{BiMo}_x\text{V}_{(1-x)}\text{O}_4$ (Fig. 2a). Clearly, diffraction patterns of low dopant concentration ($x=0.01$ and 0.015) are nearly identical to that of pristine BiVO_4 , which is in perfect agreement with monoclinic scheelite structure (JCPDS 014-0688) without any impurity phase.^{9a} Whereas for increasing Mo amount ($x=0.02$, 0.03 and 0.05), characteristic peaks of tetragonal structure (JCPDS 014-0133) at 24.6° , 32.9° , 44.0° and 48.6° were discerned,¹⁵ indicating that crystal symmetry continuously change from monoclinic to tetragonal. The crystal deformation may be ascribed to substitutional defects of Mo^{6+} ions in lieu of V^{5+} , since tetrahedral ion radii of Mo^{6+} is slightly greater than V^{5+} . As a matter of fact, with introduction of Mo, the typical crystal plane (121) and (040) in all samples gradually shift to smaller angles.¹⁶ The XRD results also confirm that Mo^{6+} has been embedded into V^{5+} sites of host BiVO_4 lattice and expedites lattice expansion. Selected area electron diffraction (SAED) patterns in Fig. 2b,c show a distinct crystal transition tendency. Excess impurities make the single crystal diffraction images intricate, which match well with the outcomes of XRD spectra.

To probe the building composition and local distortions of $\text{BiMo}_x\text{V}_{(1-x)}\text{O}_4$, Raman spectra were carried out (Fig. 2d). Raman bands at approximately 210 , 324 , 366 , 827 cm^{-1} were observed for all samples. Band centered at 210 cm^{-1} gives little structural information, just represents external mode of BiVO_4 .¹⁷ The two bands at 324 and 366 cm^{-1} are accordance

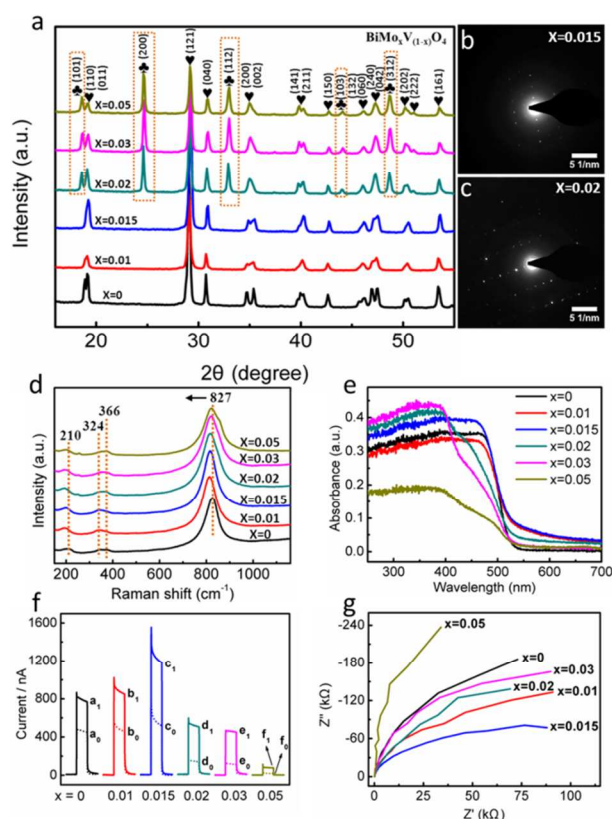


Fig. 2 a) XRD patterns of $\text{BiMo}_x\text{V}_{(1-x)}\text{O}_4$. SAED patterns of $x =$ b) 0.015 and c) 0.02. d) Raman spectra and e) The UV-vis DRS of $\text{BiMo}_x\text{V}_{(1-x)}\text{O}_4$. f) Photocurrent responses of $\text{BiMo}_x\text{V}_{(1-x)}\text{O}_4$ modified ITO electrode in the absence of (short dot curves a_0 - f_0) and present of (solid curves a_1 - f_1) $74.44 \mu\text{mol L}^{-1}$ GA. The PEC sensors were applied at 0V under 470nm light excitation in 0.1mol L^{-1} PBS (pH=7.4). g) EIS measured at 0.3 V (vs. Ag/AgCl) in 1mol L^{-1} Na_2SO_4 solution under 470nm for $\text{BiMo}_x\text{V}_{(1-x)}\text{O}_4$.

with the asymmetric-symmetric bending vibrations of the VO_4^{3-} tetrahedron.¹⁸ The dominated band at 827cm^{-1} assigned to stretching mode of V-O bonds began to shift negatively as Mo involved, which implies that local structure change is a driving force to correlate the longer V-O bond length.¹⁹

For a better overview of the electronic structure in $\text{BiMo}_x\text{V}_{(1-x)}\text{O}_4$ nanomaterials, UV-visible diffuse reflectance spectra (DRS) was applied in Fig. 2e. Apparently, while the ratio is set to 1.5% at the vanadium sites ($\text{BiMo}_{0.015}\text{V}_{0.985}\text{O}_4$), the visible light absorption property is absolute top performer. A plot of the transformed Kubelka-Munk function versus energy of light (Fig. S1, EIS†) could roughly estimate bandgap in six composites, from which the narrowest band gap energy belongs to $\text{BiMo}_{0.015}\text{V}_{0.985}\text{O}_4$.

In order to deeply understand the optoelectronic properties of $\text{BiMo}_x\text{V}_{(1-x)}\text{O}_4$, photoelectronic response trials were performed and displayed in Fig. 2f. As for bare BiVO_4 , it showed a moderate photocurrent increment (defined as PEC current, $I = I_{\text{sample}} - I_{\text{blank}} = 318.2 \text{ nA}$) at potential of 0 V with 470 nm illumination. After doping various amount of Mo, the PEC current soared to 1.23 (1.0%) and 2.09 times (1.5%) compared to pristine BiVO_4 . While the Mo mole fraction climbed to 2%, 3% and 5%, the PEC current quickly fell back. Unquestionably,

$\text{BiMo}_{0.015}\text{V}_{0.985}\text{O}_4$ demonstrates as the high-point for photocatalytic behavior. Similar tendency is also echoed by electrochemical impedance spectroscopy (EIS) plot under visible light (Fig. 2g), where $\text{BiMo}_{0.015}\text{V}_{0.985}\text{O}_4$ presents the smallest arc radius, indicating the optimum conductivity.

Since $\text{BiMo}_{0.015}\text{V}_{0.985}\text{O}_4$ manifests preferable band gap, photocurrent response and electronic transport capability, it is prone to choose the Mo mole fraction of 1.5% as optimal photosensitive constituent. Concerned explanation might be speculated as following: 1) Before the doping ratio of 1.5%, V substitution by a small amount of Mo sustains a high level of ligand π -back bonding with low d-electron count, which breaks detrimental localization of V d-orbitals due to the weak overlap with Bi 6p orbitals.²⁰ In addition, depending on the circumstance of EIS measurements in dark (Fig. S2, EIS†), the smaller resistance for $\text{BiMo}_{0.015}\text{V}_{0.985}\text{O}_4$ implies efficient improvement in photocarrier transport and extraction via Mo doping. 2) As Mo level surpasses 1.5%, photocurrent response soon slides down, even worse than the original BiVO_4 . The overload of Mo turns into carrier recombination center which further impedes the charge transport. It should be asserted that both the larger surface reactive junction area and crystallinity are essential aspects in PEC activity. Such a flower-like appearance and monoclinic scheelite structure in $\text{BiMo}_{0.015}\text{V}_{0.985}\text{O}_4$ shoulder the guarantee of desirable characteristics for antioxidants detection.

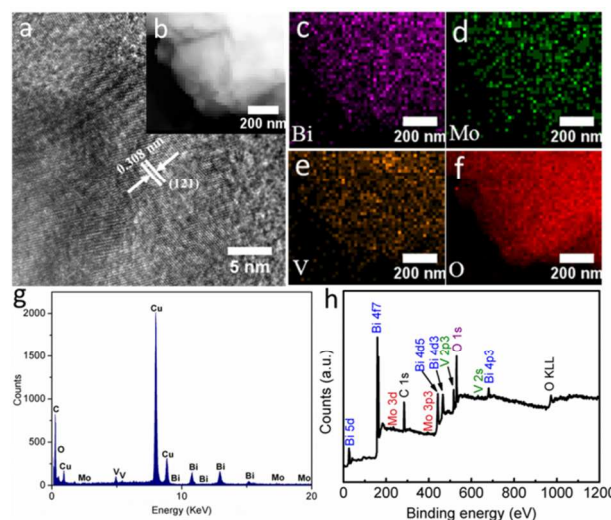


Fig. 3 a) The HETEM, b) HAADF-STEM images, Elemental mapping images of c) Bi, d) Mo, e) V and f) O, g) EDX spectrum and the survey XPS spectrum of $\text{BiMo}_{0.015}\text{V}_{0.985}\text{O}_4$.

The valuable insights into the intrinsic features of $\text{BiMo}_{0.015}\text{V}_{0.985}\text{O}_4$ were then surveyed throughly by high-resolution transmission electron microscope (HRTEM), element mapping, energy dispersive X-ray (EDX) spectrum and X-ray photoelectron spectroscopy (XPS). The interplanar spacing distance viewed from HRTEM image (Fig. 3a) reaffirms that the (121) lattice plane indwells in $\text{BiMo}_{0.015}\text{V}_{0.985}\text{O}_4$ nanocrystal. Besides, high-angle annular dark-field scanning transmission electron microscopy

(HAADF-STEM) and element mapping (Fig. 3b-f) outline that merely homogeneous Bi, Mo, V and O elements distribution, in according with the EDX (Fig. 3g) spectrum and the survey XPS (Fig. 3h). The EDX spectrum (Fig. 3g) is collected in a TECNAI G2 microscope operating at 200 kV. In fact, the C and Cu signal arise from the carbon-film-coated copper grid. The sample that we used to gather the data got closed to the edge of copper grid. Therefore, the intensity of the impurity peaks is strong. Moreover, the chemical states of $\text{BiMo}_{0.015}\text{V}_{0.985}\text{O}_4$ surfaces are showcased in Fig. S3a-c (EIS[†]). The Bi 4f peak is deconvoluted into two parts, at 159.0 and 164.3 eV, corresponding to Bi 4f_{7/2} and Bi 4f_{5/2} orbits respectively.²¹ The split peaks of Mo 3d notarized at 232.1 and 235.3 eV are severally fitted with Mo 3d_{5/2} and Mo 3d_{3/2}, suggesting that Mo cations mostly behave as Mo⁶⁺ oxidation state into the lattice of V places in $\text{BiMo}_{0.015}\text{V}_{0.985}\text{O}_4$.^{10b} Fig. S3c (EIS[†]) manifests the sole form of V⁵⁺ in VO₄³⁻, on account of the doublet peaks located at 516.9 and 524.6 eV which are separately in line with V 2p_{3/2} and V 2p_{1/2}.²²

PEC technology drives flourishing research interest as result of its inheriting merits from optical and electrochemical methods,²³ in which the selection of photoactive volunteers is of paramount importance to achieve superiority during visible photocatalysis. The contrast test applied in Fig. 4a sheds new light on favorable visible-light-responsive property of $\text{BiMo}_{0.015}\text{V}_{0.985}\text{O}_4$. It should be explained that ultrathin graphitic carbon nitride/titanium dioxide (utg-C₃N₄/TiO₂) and sulfonated graphene-TiO₂ (SGE-TiO₂) derive from previous report in our lab.^{2,24} Conspicuously, commercial titanium dioxide P25 exhibited a feeble photocurrent response (111.4 nA, curve a₀) under visible-light irradiation. Similarly, even if utg-C₃N₄ or SGE was utilized to modify TiO₂ (curve b₀ and c₀), basically there were no much differences under 470 nm. To our surprise, compared with TiO₂-based nanohybrid, $\text{BiMo}_{0.015}\text{V}_{0.985}\text{O}_4$ was easier to excite, which led to a fairly strong signal (518.6 nA, curve d₀). Moreover, upon presence of 74.44 μmol L⁻¹ GA, the photocurrent intensity of $\text{BiMo}_{0.015}\text{V}_{0.985}\text{O}_4$ greatly rise to 1183 nA (d₁), severally reaching 3.75, 3.89 and 3.11 times of P25 (a₁), utg-C₃N₄/TiO₂ (b₁) and SGE-TiO₂ (c₁). It has to admit that $\text{BiMo}_{0.015}\text{V}_{0.985}\text{O}_4$ is capable of shifting the threshold of photoresponse into visible range effectively, therefore providing feasibility for integration of low-cost antioxidant assay instruments in the near future.

For sake of AC evaluation, a novel PEC cell has been designed (Figure 1a). This device can realize a prompt signal acquisition for multiple AC assessment. During the examination, 0 V was chosen for working potential in consideration of advisable sensitivity and convenience for PEC device integration (Fig. S4, EIS[†]). Under optimum conditions, AC analysis of some standard AOs commonly found in food were accomplished, including gallic acid (GA), (-)-epicatechin (EC), chlorogenic acid (CHA), (+)-catechin hydrate (CT), caffeic acid (CA), ascorbic acid (AA), cyanidin chloride (CC) and myricetin (MT). As listed in Table S1 (EIS[†]), all of eight typical AOs expressed remarkable responses together with a

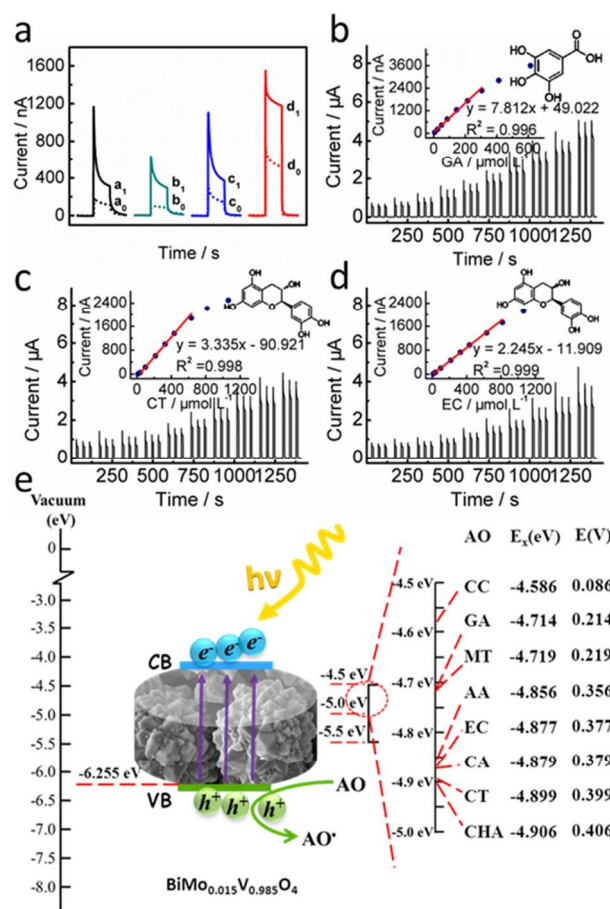


Fig. 4 a) Photocurrent responses of P25 (a₀, a₁), utg-C₃N₄/TiO₂ (b₀, b₁), SGE-TiO₂ (c₀, c₁) and $\text{BiMo}_{0.015}\text{V}_{0.985}\text{O}_4$ (d₀, d₁) modified ITO electrode without (short dots) and with (solid curves) 74.44 μmol L⁻¹ GA. Concentration-dependent photocurrent of different AOs (GA (b), CT (c) and EC (d)). The insets in b), c) and d) are the linear curves of GA, CT and EC, respectively. The PEC sensors were applied at 0 V under 470 nm light excitation in 0.1 mol L⁻¹ PBS (pH=7.4). e) Mechanism of the PEC sensor for the AC evaluation. AO: antioxidant, E_x(eV): the redox potential of AOs with respect to a vacuum, E (V): the redox potential of the AOs (vs. NHE).

wide linear range. Taking GA, CT and EC for instance, accompanied by successive addition, the PEC current presented a linear increase and then approached a plateau (Fig. 4b-d). In light of timely response for main AOs in food, global AC could be expressed as GA equivalents. Most excitingly, this conceptual strategy competently assesses comprehensive antioxidant status rather than individual AO concentration in food, which leaves much room for customers to view AC holistically. It is noticeable that after 33 times of repeated on-off detection upon 74.44 μmol L⁻¹ GA, the sensor still perceived 93.58% of the initial signal, which ensured a satisfactory reproducibility (Fig. S5, EIS[†]). Although five electrodes prepared independently were used for 74.44 μmol L⁻¹ GA assay, its relative standard deviation (RSD) was 2.95%. Given this fact, while three electrodes were stored in darkness, at least 95.50% of primitive PEC current could be picked up a month later.

Referring to correlative literatures, major AC assays are summarily divided into two categories: 1) hydrogen atom

transfer (HAT) reaction; 2) electron transfer (ET) reaction.²⁵ As depicted in Fig. 4e, the valence band (VB) of $\text{BiMo}_{0.015}\text{V}_{0.985}\text{O}_4$ was calculated to be -6.255 eV by virtue of Mott-Scotcky plot (Fig. S7, EIS†) and plot of transformed Kubelka-Munk function versus the energy (Fig. S1, EIS†), which is likely to oxidize water molecules to generate hydroxyl radicals. Once radicals accumulate, terephthalic acid (TA) can scavenge them with relevant phenomenon reflecting in fluorescence spectrum.²⁶ What is surprised that the fluorescence peak situated at 425 nm (Fig. S6, EIS†) was hardly discovered any difference as time went on. Hence, this system should be classified as an ET process on basis of direct reaction between AOs and trapped holes. An in-depth perspective into PEC mechanism is postulated as the following: Except that inert lattice mismatching in $\text{BiMo}_{0.015}\text{V}_{0.985}\text{O}_4$ may compensate slow carrier mobility, Mo serves as shallow donors to make excess electrons form small polarons around reduced V^{4+} centers.²⁷ A multitude of polarons help charge migrating to an adjacent V^{5+} site and render potent overlap at large scale. Undoubtedly, it weakens the hopping activation energy for unconnected V neighbors, thereby minimizing inner resistance and facilitating electron transport. In this sense, composition regulation and morphology innovation endow $\text{BiMo}_{0.015}\text{V}_{0.985}\text{O}_4$ with suitable band alignment to easily absorb visible light. Thereupon, electrons excited in the VB will transfer to the CB, leaving holes behind. The high-energy electrons promptly arrive at the ITO surface, which eventually gives rise to remarkable photocurrent output. As expressed in Fig. S8 (EIS†), the CB and VB locations of $\text{BiMo}_{0.015}\text{V}_{0.985}\text{O}_4$ bestride the formal potential of eight AOs. Aside from electrolyte, if AOs exist in the solution, positive charge holes are apt to be replenished by electrons from AOs and fleetly get ready for the next photoexcitation. By feat of this unique regenerative ability, the amplified signal can be utilized for overall AC assessment.

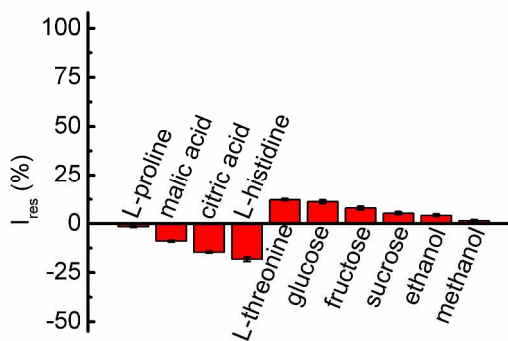


Fig. 5 Photocurrent responses of $\text{BiMo}_{0.015}\text{V}_{0.985}\text{O}_4$ modified ITO electrode upon the addition of 10 mmol L^{-1} of L-malic acid, or 20 mmol L^{-1} of L-citric acid, or 25 mmol L^{-1} of L-threonine, or 40 mmol L^{-1} each of glucose, fructose, or 50 mmol L^{-1} of L-histidine, or 250 mmol L^{-1} each of L-proline, sucrose, ethanol, methanol in 0.1 mol L^{-1} PBS (pH=7.4) containing 0.5 mmol L^{-1} GA at 0V under 470nm light excitation.

With respect to a complex food system, coexistent substances always emerge, such as amino acids, polysaccharose and organic acid. Attributing to actual situation, a tentative trial was inspected, which contains 0.5 mmol L^{-1} GA accompanied

with some interfering components (Fig. 5). Evidently, insignificant photocurrent decay was seen when 500 folds of L-proline, sucrose, ethanol and methanol, 100 folds of L-histidine, 80 folds of glucose and fructose, 50 folds of L-threonine, 40 folds of L-citric acid, 20 folds of L-malic acid were involved. Standing on this point, the PEC transducer embodies a pretty universality towards practical applications.

Table 1 The antioxidant capacities of fresh fruits as found with our PEC sensor, the Folin-Ciocalteu (F-C) and the DPPH method, respectively. Data are expressed in mg L^{-1} for fruits. (n = 3)









Practical Samples	PEC sensor	F-C method	DPPH method
	356.38 ± 6.80	369.73 ± 2.63	267.61 ± 1.46
	229.40 ± 1.13	247.71 ± 0.61	172.73 ± 2.92
	257.45 ± 4.95	252.01 ± 2.43	176.86 ± 2.53
	265.54 ± 6.63	308.44 ± 5.27	182.01 ± 3.86
	104.18 ± 3.14	129.27 ± 0.38	83.76 ± 0.73
	445.59 ± 9.12	468.67 ± 1.52	281.66 ± 1.82
	540.48 ± 1.01	564.39 ± 3.04	325.50 ± 3.16
	601.12 ± 5.38	611.73 ± 4.56	344.83 ± 11.38

Table 2 The antioxidant capacities of commercial teas (T) and drinks (D) as found with our PEC sensor, the Folin-Ciocalteu (F-C) and the DPPH method, respectively. Data are expressed in mg g^{-1} for teas and in mg L^{-1} for drinks. (n = 3)

Practical Samples	PEC Sensor	F-C Method	DPPH Method
T1	18.78 ± 0.80	35.82 ± 0.25	54.84 ± 0.24
T2	73.33 ± 1.72	106.56 ± 0.53	144.03 ± 0.42
T3	108.63 ± 1.91	120.87 ± 0.70	161.18 ± 0.85
T4	52.11 ± 1.51	71.60 ± 0.23	106.90 ± 0.73
D1	387.19 ± 0.62	420.30 ± 1.07	203.64 ± 2.39
D2	345.31 ± 1.24	386.24 ± 6.77	193.31 ± 2.30
D3	396.16 ± 4.34	437.52 ± 1.32	318.36 ± 7.59
D4	429.88 ± 4.24	459.78 ± 2.97	325.78 ± 2.39
D5	316.78 ± 0.98	337.46 ± 2.21	185.21 ± 1.53
D6	393.10 ± 0.98	435.85 ± 1.14	250.63 ± 4.08
D7	457.50 ± 3.01	492.08 ± 1.14	566.88 ± 3.28
D8	712.10 ± 13.04	770.78 ± 1.02	731.51 ± 1.55
D9	641.11 ± 9.59	701.33 ± 3.70	728.08 ± 1.37
D10	436.60 ± 4.37	487.50 ± 0.41	522.16 ± 4.07
D11	296.41 ± 0.76	310.27 ± 1.70	164.06 ± 2.06
D12	352.02 ± 5.05	388.18 ± 0.62	198.06 ± 2.06
D13	391.22 ± 1.42	432.17 ± 1.03	232.09 ± 4.07
D14	176.01 ± 0.76	137.02 ± 0.52	45.29 ± 1.63
D15	58.07 ± 0.36	34.43 ± 0.19	27.96 ± 0.73
D16	59.29 ± 0.27	40.32 ± 0.18	31.07 ± 0.48

The feasibility of rational AC estimation is further pursued upon different foodstuffs. Eight kinds of fresh fruits as natural food have been firstly explored (Table1). For these samples, the juice extracts were gathered and centrifuged before detection. Besides natural food, this PEC strategy is also available for the processed food such as tea, wine, coffee, drinks, etc. In this study, some different commercial teas and beverages were analysed as examples (Table 2, Table S2, EIS†). To investigate

the reliability of the PEC platform, F-C and DPPH approaches as experienced optical means were simultaneously carried out. As is well known that the outcome gaps between PEC and DPPH methods should lie in different mechanism and calibration standard. Likewise, although PEC and F-C measurements are both grouped into the ET reaction and take GA as an equivalent, the final test results of PEC assay often present relatively small values. On behalf of colorimetric total phenolics analysis, F-C method is inclined to be interfered by exterior colors, reducing agents and possibly metal chelators. As for dark-colored systems, F-C detection might make a big discount of precision. In contrast, PEC sensor adopts back-side illumination to avoid background color effect, thereby attaining a more reasonable accuracy. Despite all of that, it is found from Table 1 and Table 2, the data tendency of PEC, F-C and DPPH were exactly consistent with each other. For the superiority of high sensitivity, convenient operability and outstanding anti-interference, the PEC platform is thus undertaken as efficient criterion for evaluation of antioxidant nutrient towards food.

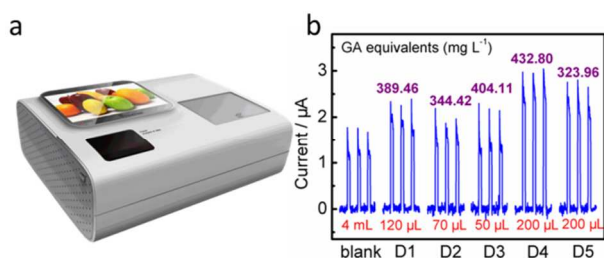


Fig. 6 a) Photograph of integrated PEC platform. b) Photocurrent responses of $\text{BiMo}_{0.015}\text{V}_{0.985}\text{O}_4$ modified ITO electrode in integrated PEC platform without (blank PBS solution) and with addition of a certain volume juices to 4 mL 0.1 mol L^{-1} PBS (pH=7.4).

To date, research and development upon commercial PEC apparatus for AOs analysis are almost in infancy. After unremitting efforts, we have accomplished integration of a homegrown device embedded with testing system, data collection & processing and information output units (Fig. 6a and Fig. S9, ESI†). The internal flow-cell system acquired the linear regression equation of GA, namely, y (μA) = $0.01056C$ ($\mu\text{mol L}^{-1}$) – 0.09377 ($R^2 = 0.998$). When five of the above-mentioned commercial drinks were examined, each of photocurrent response from homegrown device was found in good consistency with calculative values of PEC sensors (Fig. 6b, Table 2). Of course, the embedded equipment is highly robust and automatic that meets the requirement of “smart” AC assessment for layfolk.

Conclusions

In summary, diminutive lattice and morphology variations of Mo-doped BiVO_4 have an immediate effect on the photoactivity. With the aid of adjustable impurity doping, flower-like $\text{BiMo}_{0.015}\text{V}_{0.985}\text{O}_4$ explicitly exerts great advantages in prompt communication with AOs. The ultrasensitive $\text{BiMo}_{0.015}\text{V}_{0.985}\text{O}_4$ based PEC platform has blossomed into a versatile format to estimate AC in food. Based on this principle,

an engineering fluidic device was exploited for the real-time diagnosis of dietary antioxidant samples against a set of healthy controls. The integrated device highlights rapid response, long-lasting stability, anti-interference and universality for “smart” AC analysis, especially meet the approval of personnels without highly trained experiences. This proof-of-concept implementation is seen as a giant step for progressively intelligent mobile terminal combination detection in foodstuff industries, even opening up a bright prospect for cosmetic and healthcare supervision.

Acknowledgements

This work was supported by NSFC, China (21225524, and 21475122 and 21205112) and the Department of Science and Techniques of Jilin Province (20150203002YY, 20150201001GX and SYHZ0006) and Chinese Academy of Sciences (YZ201354, YZ201355).

Notes and references

^a State Key Laboratory of Electroanalytical Chemistry, c/o Engineering Laboratory for Modern Analytical Techniques, Changchun Institute of Applied Chemistry, Changchun, Jilin 130022, P. R. China. E-mail: dxhan@ciac.ac.cn, Fax: (+)86-431-85262800, Tel: (+)86-431-85262425.

^b University of Chinese Academy of Sciences, Beijing 100039, P. R. China

^c Shenyang Agricultural University, Shenyang 110161, P. R. China

† Electronic Supplementary Information (ESI) available: Detailed materials and methods; The plot of transformed Kubelka-Munk function versus the energy of light; EIS plots in dark; XPS spectrum; potential optimization; Photocurrent response reproducibility in PEC cell; fluorescence emission spectra; Mott-Schottky plot; CV of antioxidants; linear equations, linear ranges and correlation coefficients for antioxidants; different species of processed food analyzed. See DOI: 10.1039/b000000x/

- a) S. Gorjanovic, D. Komes, F. T. Pastor, A. Belscak-Cvitanovic, L. Pezo, I. Hecimovic and D. Suznjevic, *J. Agr. Food Chem.*, 2012, **60**, 9573-9580; b) A. N. Tufan, S. Baki, K. Guclu, M. Ozyurek and R. Apak, *J. Agr. Food Chem.*, 2014, **62**, 7111-7117; c) A. Haber, M. Aviram and Z. Gross, *Chem. Sci.*, 2011, **2**, 295-302.
- W. Ma, D. Han, M. Zhou, H. Sun, L. Wang, X. Dong and L. Niu, *Chem. Sci.*, 2014, **5**, 3946-3951.
- a) J. Gan, X. Lu and Y. Tong, *Nanoscale*, 2014, **6**, 7142-7164; b) M. Barroso, S. R. Pendlebury, A. J. Cowan and J. R. Durrant, *Chem. Sci.*, 2013, **4**, 2724-2734.
- Y. H. Ng, A. Iwase, A. Kudo and R. Amal, *J. Phys. Chem. Lett.*, 2010, **1**, 2607-2612.
- a) P. Roy, S. Berger and P. Schmuki, *Angew. Chem. Int. Ed.*, 2011, **50**, 2904-2939; b) J. Tang, B. Kong, Y. Wang, M. Xu, Y. Wang, H. Wu and G. Zheng, *Nano Lett.*, 2013, **13**, 5350-5354.
- a) X. Gao, H. B. Wu, L. Zheng, Y. Zhong, Y. Hu and X. W. Lou, *Angew. Chem. Int. Ed.*, 2014, **53**, 5917-5921; b) T. W. Kim and K.-S. Choi, *Science*, 2014, **343**, 990-994; c) P. M. Rao, L. Cai, C. Liu, I. S. Cho, C. H. Lee, J. M. Weiss, P. Yang and X. Zheng, *Nano Lett.*, 2014, **14**, 1099-1105; d) Y. Zhao, Y. Xie, X. Zhu, S. Yan and S. Wang, *Chem. Eur. J.*, 2008, **14**, 1601-1606; e) Y. Ma, S. R. Pendlebury, A. Reynal, F. Le Formal and J. R. Durrant, *Chem. Sci.*, 2014, **5**, 2964-2973.
- a) B. Cheng, W. Wang, L. Shi, J. Zhang, J. Ran and H. Yu, *International Journal of Photoenergy*, 2012, DOI: 10.1155/2012/797968; b) M. Han, X. Chen, T. Sun, O. K. Tan and M. S. Tse, *CrystEngComm*, 2011, **13**, 6674-6679; c) Y. Liu, H. Dai, J. Deng, L. Zhang and C. T. Au, *Nanoscale*,

- 2012, **4**, 2317-2325; d)H. Luo, A. H. Mueller, T. M. McCleskey, A. K. Burrell, E. Bauer and Q. X. Jia, *J. Phys. Chem. C*, 2008, **112**, 6099-6102.
- 8 a)Y. Park, K. J. McDonald and K.-S. Choi, *Chem. Soc. Rev.*, 2013, **42**, 2321-2337; b)D. K. Zhong, S. Choi and D. R. Gamelin, *J. Am. Chem. Soc.*, 2011, **133**, 18370-18377.
- 9 a)W. J. Jo, J.-W. Jang, K.-j. Kong, H. J. Kang, J. Y. Kim, H. Jun, K. P. S. Parmar and J. S. Lee, *Angew. Chem. Int. Ed.*, 2012, **51**, 3147-3151; b)C. Li, S. Wang, T. Wang, Y. Wei, P. Zhang and J. Gong, *Small*, 2014, **10**, 2783-2790; c)M. Xie, X. Fu, L. Jing, P. Luan, Y. Feng and H. Fu, *Adv. Energy Mater.*, 2014, **4**.
- 10 a)Z.-F. Huang, L. Pan, J.-J. Zou, X. Zhang and L. Wang, *Nanoscale*, 2014, **6**, 14044-14063; b)S. K. Pilli, T. E. Furtak, L. D. Brown, T. G. Deutsch, J. A. Turner and A. M. Herring, *Energy Environ. Sci.*, 2011, **4**, 5028-5034; c)L. Zhang, C.-Y. Lin, V. K. Valev, E. Reisner, U. Steiner and J. J. Baumberg, *Small*, 2014, **10**, 3970-3978; d)W. Luo, Z. Li, T. Yu and Z. Zou, *J. Phys. Chem. C*, 2012, **116**, 5076-5081.
- 11 a)K. E. Kweon and G. S. Hwang, *Phys. Rev. B*, 2013, **87**; b)W. Luo, J. Wang, X. Zhao, Z. Zhao, Z. Li and Z. Zou, *Phys. Chem. Chem. Phys.*, 2013, **15**, 1006-1013; c)L. Zhang, E. Reisner and J. J. Baumberg, *Energy Environ. Sci.*, 2014, **7**, 1402-1408.
- 12 a)D. Eisenberg, H. S. Ahn and A. J. Bard, *J. Am. Chem. Soc.*, 2014, **136**, 14011-14014; b)H. S. Park, K. E. Kweon, H. Ye, E. Paek, G. S. Hwang and A. J. Bard, *J. Phys. Chem. C*, 2011, **115**, 17870-17879.
- 13 S. Obregon, S. W. Lee and G. Colon, *Dalton. Trans.*, 2014, **43**, 311-316.
- 14 a)G. Tan, L. Zhang, H. Ren, S. Wei, J. Huang and A. Xia, *ACS Appl. Mater. Interfaces*, 2013, **5**, 5186-5193; b)L. Zhou, W. Wang, L. Zhang, H. Xu and W. Zhu, *J. Phys. Chem. C*, 2007, **111**, 13659-13664.
- 15 X. Zhang, Z. Ai, F. Jia, L. Zhang, X. Fan and Z. Zou, *Mater. Chem. Phys.*, 2007, **103**, 162-167.
- 16 C. Yin, S. Zhu, Z. Chen, W. Zhang, J. Gu and D. Zhang, *J. Mater. Chem. A*, 2013, **1**, 8367-8378.
- 17 Y. Wang, W. Wang, H. Mao, Y. Lu, J. Lu, J. Huang, Z. Ye and B. Lu, *ACS Appl. Mater. Interfaces*, 2014, **6**, 12698-12706.
- 18 J. Yu and A. Kudo, *Adv. Funct. Mater.*, 2006, **16**, 2163-2169.
- 19 A. J. E. Rettie, H. C. Lee, L. G. Marshall, J.-F. Lin, C. Capan, J. Lindemuth, J. S. McCloy, J. Zhou, A. J. Bard and C. B. Mullins, *J. Am. Chem. Soc.*, 2013, **135**, 11389-11396.
- 20 J. K. Cooper, S. Gul, F. M. Toma, L. Chen, P.-A. Glans, J. Guo, J. W. Ager, J. Yano and I. D. Sharp, *Chem. Mater.*, 2014, **26**, 5365-5373.
- 21 M. Zhong, T. Hisatomi, Y. Kuang, J. Zhao, M. Liu, A. Iwase, Q. Jia, H. Nishiyama, T. Minegishi, M. Nakabayashi, N. Shibata, R. Niishiro, C. Katayama, H. Shibano, M. Katayama, A. Kudo, T. Yamada and K. Domen, *J. Am. Chem. Soc.*, 2015, **137**, 5053-5060.
- 22 H. Li, Y. Sun, B. Cai, S. Gan, D. Han, L. Niu and T. Wu, *Appl. Catal. B: Environ.*, 2015, **170**, 206-214.
- 23 a)W. Ma, L. Wang, N. Zhang, D. Han, X. Dong and L. Niu, *Anal. Chem.*, 2015, **87**, 4844-4850; b)W.-W. Zhao, Z.-Y. Ma, P.-P. Yu, X.-Y. Dong, J.-J. Xu and H.-Y. Chen, *Anal. Chem.*, 2012, **84**, 917-923.
- 24 L. Wang, W. Ma, S. Gan, D. Han, Q. Zhang and L. Niu, *Anal. Chem.*, 2014, **86**, 10171-10178.
- 25 a)R. Apak, K. Gueclue, B. Demirata, M. Oezyuerek, S. E. Celik, B. Bektasoglu, K. I. Berker and D. Oezyurt, *Molecules*, 2007, **12**, 1496-1547; b)Q. Guo, S. Ji, Q. Yue, L. Wang, J. Liu and J. Jia, *Anal. Chem.*, 2009, **81**, 5381-5389; c)P. Li, W. Zhang, J. Zhao, F. Meng, Q. Yue, L. Wang, H. Li, X. Gu, S. Zhang and J. Liu, *Analyst*, 2012, **137**, 4318-4326.
- 26 a)S. Kohtani, K. Yoshida, T. Maekawa, A. Iwase, A. Kudo, H. Miyabe and R. Nakagaki, *Phys. Chem. Chem. Phys.*, 2008, **10**, 2986-2992; b)W. Ma, D. Han, S. Gan, N. Zhang, S. Liu, T. Wu, Q. Zhang, X. Dong and L. Niu, *Chem. Commun.*, 2013, **49**, 7842-7844; c)Q. Yue, K. Zhang, X. Chen, L. Wang, J. Zhao, J. Liu and J. Jia, *Chem. Commun.*, 2010, **46**, 3369-3371.
- 27 M. Zhou, J. Bao, Y. Xu, J. Zhang, J. Xie, M. Guan, C. Wang, L. Wen, Y. Lei and Y. Xie, *ACS Nano*, 2014, **8**, 7088-7098.